Journal of Engineering Mathematics **42:** 1–22, 2002.

A numerical study of pulsatile blood flow in an eccentric catheterized artery using a fast algorithm

PRABIR DARIPA* and RANJAN K. DASH†
Department of Mathematics, Texas A&M University, College Station, TX–77843, U.S.A.

Received 7 August 2000; accepted in revised form 8 June 2001

Abstract. The pulsatile blood flow in an eccentric catheterized artery is studied numerically by making use of an extended version of the fast algorithm of Borges and Daripa [J. Comp. Phys., 2001]. The mathematical model involves the usual assumptions that the arterial segment is straight, the arterial wall is rigid and impermeable, blood is an incompressible Newtonian fluid, and the flow is fully developed. The flow rate (flux) is considered as a periodic function of time (prescribed). The axial pressure gradient and velocity distribution in the eccentric catheterized artery are obtained as solutions of the problem. Through the computed results on axial pressure gradient, the increases in mean pressure gradient and frictional resistance in the artery due to catheterization are estimated. These estimates can be used to correct the error involved in the measured pressure gradients using catheters.

Key words: Poisson solver, fast algorithm, pulsatile blood flow, eccentric catheterized artery.

1. Introduction

Catheters are of extensive use in contemporary medical science. Typically, a catheter consists of a long flexible cylindrical tube at the tip of which various functional tools (*e.g.*, pressure transducers, flow meters, inflatable balloons, etc.) are positioned. The principle is to insert the catheter-tool device into a peripheral artery and then to position the device in the desired part of the arterial network by passing an appropriate length of the catheter through the artery. These catheter-tool devices are usually used for the measurement of various physiological flow characteristics (*e.g.*, arterial blood pressure or pressure gradient and flow velocity or flow rate) as well as for the diagnosis (*e.g.*, X-ray angiography and intravascular ultrasound) and treatment (*e.g.*, coronary balloon angioplasty) of various arterial diseases (see [1–6] for details).

The insertion of a catheter into an artery leads to the formation of an annular region between the catheter wall and the arterial wall. This alters the flow field and disturbs the hemodynamic conditions in the artery that existed before the catheterization. In fact, this results in an increase in frictional resistance to flow through the artery and modifies the pressure distribution. Therefore, the pressure or the pressure gradient recorded by the transducer attached to the catheter differs from that of an uncatheterized artery. In order to obtain an accurate pressure reading, it is essential to know the catheter-induced errors. This necessitates to study the Navier–Stokes equations governing the flow of blood in catheterized arteries.

*Author for correspondence (e-mail: Prabir.Daripa@math.tamu.edu).
†Present address: National Simulation Resource, Department of Bioengineering, Box 357962, University of Washington, Seattle, WA-98195, U.S.A.

In a series of papers, Petterson and co-workers [7–11] studied extensively the hydro- and hemodynamic effects of catheterization of vessels with and without stenosis by the help of various experimental models. Through a detailed mathematical model, MacDonald [12] studied the pulsatile blood flow in a catheterized artery and obtained theoretical estimates for pressure-gradient corrections for catheters which are positioned eccentrically as well as coaxially with the artery. Back [2] and Back *et al.* [3, 4], using analytical flow modeling coupled with *in vitro* experimental evidence and angiographic data, studied the important hemodynamical characteristics like the wall shear stress, pressure drop, and frictional resistance in a catheterized coronary artery under normal as well as the pathological situation of a stenosis present and estimated the mean-flow resistance increase due to catheterization for concentric and eccentric catheter configurations.

Taking into account the non-Newtonian behavior of blood described by the Casson fluid model, Dash *et al.* [13] studied the changed flow pattern (both steady and pulsatile) in a narrow artery when a catheter is inserted into it and estimated the increase in frictional resistance in the artery due to catheterization. Taking into account the steady streaming effect, Sarkar and Jayaraman [14] studied the pulsatile flow in a catheterized stenosed artery and estimated the correction in the mean pressure drop along the stenosis due to catheterization. The effect of catheterization on various flow characteristics in a curved artery with or without stenosis was studied by Karahalios [15], Jayaraman and Tiwari [16], Dash *et al.* [17], and Jayaraman and Dash [18].

In this paper, we study the pulsatile flow of blood in a straight eccentric catheterized artery by modeling blood as an incompressible Newtonian fluid. MacDonald [12] has originally studied this problem analytically using perturbation and asymptotic methods. This problem is revisited here for the reasons mentioned below. The related steady fully developed flow of incompressible Newtonian fluids in an eccentric annulus has been studied analytically by Heyda [19], Snyder and Goldstein [20], and MacDonald [21].

One of the objectives of the paper is to extend the fast algorithm of Borges and Daripa [22] (see also [23] and [24] for more details) for solving the Poisson equation inside a circular disk to an annular domain, and to implement and apply the extended fast algorithm to solve an applied physical problem. The problem of pulsatile blood flow in an eccentric catheterized artery is chosen here since the flow domain is of an annular configuration and the analytic solution to the problem is known from the study of MacDonald [12] for small and large values of the eccentricity parameter. Using this fast algorithm, we have proposed an iterative numerical scheme to compute accurately and rapidly the flow characteristics (*i.e.*, the axial pressure gradient and velocity distribution) in the eccentric catheterized artery. The computed results on axial pressure gradient for several values of the Womersley frequency parameter α, radii ratio a, and eccentricity parameter c have been used to estimate the increases in mean pressure gradient and frictional resistance in the artery due to catheterization.

The layout of the paper is as follows. The details of the mathematical formulation of the problem and the method of solution are presented in Sections 2 and 3, respectively. Since the flow is pulsatile, the flow rate $Q(t)$ is assumed to be a prescribed periodic function of time t. The solutions for the axial pressure gradient $\partial p/\partial z(t)$ and velocity distribution $w(x, y, t)$ are then written as Fourier series with complex Fourier coefficients P_j and $w_j(x, y)$, respectively. In the Fourier space, the problem is then reduced to solving a Helmholtz equation for each $w_j(x, y)/P_j$ with Dirichlet conditions on the boundaries. The real and imaginary parts of each of these Helmholtz equations are coupled Poisson equations. A suitable conformal mapping is used which transforms the eccentric annular domain into a concentric annular domain. The

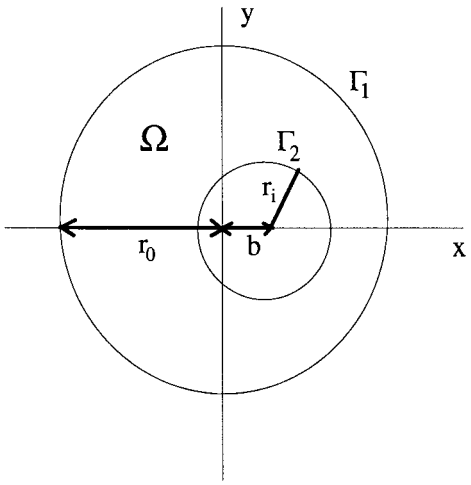

Figure 1. Schematic diagram of a cross-sectional plane of the eccentric catheterized artery.

transformed coupled Poisson equations in this concentric annular domain are then solved by use of an iterative numerical scheme and a fast algorithm. In Section 4, we present a fast algorithm to solve a Poisson equation in an annular disk with Dirichlet conditions on the boundaries by modifying the fast algorithm of Borges and Daripa [22] for solving Dirichlet and Neumann problems inside a circular disk. This Poisson solver is then used to solve the coupled Poisson equations presented in Subsection 3.3. The case of zero eccentricity is dealt with separately in the Appendix. In Section 5, the numerical results are discussed and the estimates for the increased mean pressure gradient and frictional resistance are made. The concluding remarks are presented in Section 6.

2. Mathematical formulation

Figure 1 shows a typical cross-section of the eccentric catheterized artery. It is an eccentric annular region Ω bounded by $\partial\Omega = \Gamma_1 \cup \Gamma_2$ where

$$\Gamma_1 :\ x^2 + y^2 = r_0^2 \quad \text{and} \quad \Gamma_2 : /\ (x-b)^2 + y^2 = r_i^2. \tag{2.1}$$

Here r_0 and r_i are the radii of the outer (artery) and inner (catheter) tubes, respectively. The origin $(0, 0)$ of the coordinate system is chosen as the center of the outer tube and the x-axis is chosen to pass through the center of the inner tube in the cross-sectional plane. We denote the center of the inner tube by $(b, 0)$ with b a constant. The fluid (blood) is considered to be incompressible and Newtonian, and the flow is assumed to be due to a pulsatile (oscillatory) axial pressure gradient $\partial p/\partial z(t)$ with period $2\pi/\omega$. We denote the velocity field as $(0, 0, w)$. It is further assumed that the artery and the catheter are infinitely long and the pressure-sensing device is mounted on the catheter at a large distance upstream from the tip of the catheter, so that the effects of entrance and the catheter tip can be neglected. In this case, the flow can be considered as laminar and fully developed. Since the flow is axial (*i.e.*, in the z-direction), the only non-zero stress components are τ_{xz} and τ_{yz}. Therefore, the simplified Navier-Stokes equation and the no-slip boundary conditions governing the flow (see [12]) are given by

$$\rho\frac{\partial w}{\partial t} = -\frac{\partial p}{\partial z} + \mu\left[\frac{\partial^2 w}{\partial x^2} + \frac{\partial^2 w}{\partial y^2}\right] \quad \text{in} \quad \Omega \tag{2.2}$$

and

$$w = 0 \quad \text{on} \quad \partial\Omega, \tag{2.3}$$

where ρ and μ are the density and viscosity of the fluid, respectively. It is convenient to work with non-dimensional variables. Therefore, we introduce the characteristic length as r_0, characteristic pressure gradient as $-P_g$ (mean pressure gradient), characteristic velocity as $P_g r_0^2/\mu$, and the characteristic time as ω^{-1}. In non-dimensional form, Equations (2.1) and (2.2) are reduced to

$$\alpha^2 \frac{\partial w}{\partial t} = \frac{\partial p}{\partial z} + \frac{\partial^2 w}{\partial x^2} + \frac{\partial^2 w}{\partial y^2} \quad \text{in} \quad \Omega \tag{2.4}$$

and

$$w = 0 \quad \text{on} \quad \partial\Omega, \tag{2.5}$$

where $\alpha = \sqrt{r_0^2 \omega/(\frac{\mu}{\rho})}$ is the Womersley frequency parameter. The boundary curves Γ_1 and Γ_2, in non-dimensional form, are reduced to

$$\Gamma_1 : \; x^2 + y^2 = 1 \quad \text{and} \quad \Gamma_2 : / \; (x - c)^2 + y^2 = a^2, \tag{2.6}$$

where $a = r_i/r_0$ and $c = b/r_0$. During flow simulation in a catheterized artery, it is often desirable to estimate the increase in axial pressure gradient due to the insertion of a catheter into an artery. In this case, the flux (flow rate) is assumed to be known (constant) which can be expressed in the form of a Fourier series:

$$Q(t) = \iint_{\Omega} w(x, y, t) \, \mathrm{d}x \, \mathrm{d}y = \sum_{j=-\infty}^{\infty} Q_j \mathrm{e}^{\mathrm{i}jt}, \tag{2.7}$$

where $\mathrm{i} = \sqrt{-1}$. The flow-rate is non-dimensionalized with respect to the characteristic flow rate $P_g r_0^4/\mu$. The problem for the case of zero eccentricity (*i.e.*, $c = 0$) is dealt with separately in the Appendix.

3. Method of solution

Since the flow rate $Q(t)$ is a periodic function of time t (prescribed), we seek the solutions for $\frac{\partial p}{\partial z}(t)$ and $w(x, y, t)$ in the form of Fourier series

$$\frac{\partial p}{\partial z}(t) = \sum_{j=-\infty}^{\infty} P_j \mathrm{e}^{\mathrm{i}jt} \quad \text{and} \quad w(x, y, t) = \sum_{j=-\infty}^{\infty} w_j(x, y) \mathrm{e}^{\mathrm{i}jt}. \tag{3.1}$$

Substituting the series (3.1) in the Dirichlet problem consisting of the Equations (2.4) and (2.5) and equating the coefficients of $\mathrm{e}^{\mathrm{i}jt}$ on both the sides, we get the Dirichlet problem

$$\frac{\partial^2 E_j}{\partial x^2} + \frac{\partial^2 E_j}{\partial y^2} = \mathrm{i}\gamma_j E_j - 1 \quad \text{in} \quad \Omega \tag{3.2}$$

and

$$E_j = 0 \quad \text{on} \quad \partial\Omega, \tag{3.3}$$

for $j = 0, \pm 1, \pm 2, \cdots, \pm\infty$. Here

$$E_j(x, y) = \frac{w_j(x, y)}{P_j} \quad \text{and} \quad \gamma_j = j\alpha^2. \tag{3.4}$$

It can be easily shown that the coefficients E_j's satisfy

$$E_j = \overline{E_{-j}} \quad \text{for} \quad j = \pm 1, \pm 2, \ldots, \pm\infty. \tag{3.5}$$

It is worth noting here that Equation (3.2) is a complex Helmholtz equation for the complex coefficient E_j. Solving the Dirichlet problem (3.2) and (3.3) provides E_j which can be used, as described below, to obtain the axial pressure gradient in the eccentric annulus.

Note: We note that the axial pressure gradient has at least the same degree of regularity as the two dimensional Laplacian of axial velocity in Equation (2.4). Therefore, the axial velocity w is more regular than the axial pressure gradient $\partial p/\partial z$, and hence, the Fourier coefficients w_j decay more rapidly than the Fourier coefficients P_j (see Equation (3.1)). This guarantees the existence of the function E_j for all j as defined in Equation (3.4).

3.1. Evaluation of pressure gradient

Substituting the expression (3.1) for $w(x, y, t)$ in Equation (2.7) and equating the coefficient of e^{ijt} on both the sides, we get

$$\iint_{\Omega} w_j(x, y)\, dx\, dy = Q_j, \tag{3.6}$$

which gives

$$P_j = Q_j \Big/ \iint_{\Omega} E_j(x, y)\, dx\, dy, \tag{3.7}$$

for $j = 0, \pm 1, \pm 2, \pm\infty$. The axial pressure gradient in the eccentric annulus can be obtained through Equations (3.1) and (3.7).

In the following subsection, we describe our approach for solving the Dirichlet problem consisting of the complex Helmholtz equation (3.2) and boundary condition (3.3) in the eccentric annular domain Ω. In order to take advantage of the recently developed fast solvers (see Section 4) for real elliptic problems which are well suited for concentric circles, we first conformally transform the eccentric annular domain Ω into a concentric annular domain D and then transform the complex Helmholtz equation into a two coupled Poisson equations. We discuss this procedure next.

3.2. Conformal mapping

It is easy to see that the conformal mapping (see [21, 12])

$$\xi = f(z) = \frac{z - \beta_1}{z - 1/\beta_1}, \tag{3.8}$$

maps the circles $\Gamma_1 : |z| = 1$ and $\Gamma_2 : |z - c| = a$ into the circles $\partial D_1 : |\xi| = \beta_1$ and $\partial D_2 : |\xi| = \beta_2$, respectively, where β_1 is the smallest real root of the quadratic algebraic equation

$$cs^2 + (a^2 - c^2 - 1)s + c = 0, \tag{3.9}$$

and

$$\beta_2 = \sqrt{\frac{\beta_1(\beta_1 - c)}{1 - \beta_1 c}}. \tag{3.10}$$

It is easy to check that, if $c > 0$ and $a + c < 1$, then

$$0 < c < \beta_1 < a + c < 1 \quad \text{and} \quad 0 < \beta_2 < \beta_1. \tag{3.11}$$

Therefore, the eccentric annular region Ω bounded by the circles Γ_1 and Γ_2 in the z-plane is mapped onto the concentric annular region D bounded by $\partial D = \partial D_1 \cup \partial D_2$ in the ξ-plane. If we write $\xi = r\mathrm{e}^{\mathrm{i}\theta}$, then the conformal mapping (3.8) transforms the Dirichlet problem (3.2) and (3.3) into

$$\Delta E_j = F(r, \theta)(\mathrm{i}\gamma_j E_j - 1) \quad \text{in} \quad D \tag{3.12}$$

and

$$E_j = 0 \quad \text{on} \quad \partial D, \tag{3.13}$$

where the Laplacian Δ and the function $F(r, \theta)$ are defined, by

$$\Delta = \frac{\partial^2}{\partial r^2} + \frac{1}{r}\frac{\partial}{\partial r} + \frac{1}{r^2}\frac{\partial^2}{\partial \theta^2} \tag{3.14}$$

and

$$F(r, \theta) = \left| \frac{\beta_1^2 - 1}{\beta_1(\xi - 1)^2} \right|^2 = \frac{(\beta_1^2 - 1)^2}{\beta_1^2(1 - 2r\cos\theta + r^2)^2}, \tag{3.15}$$

respectively. The expression (3.7) for the Fourier coefficient P_j is transformed into

$$P_j = Qj \Big/ \int_0^{2\pi} \int_{\beta_2}^{\beta_1} F(r, \theta) E_j(r, \theta) r \, \mathrm{d}r \, \mathrm{d}\theta. \tag{3.16}$$

3.3. Precise mathematical problem and numerical scheme

For convenience, we write the function $E_j(r, \theta)$ in the form

$$E_j(r, \theta) = G_j(r, \theta) + \mathrm{i}H_j(r, \theta). \tag{3.17}$$

Then the Dirichlet problem (3.12) and (3.13) is reduced to

$$\Delta G_j = -F(r, \theta)(\gamma_j H_j + 1), \qquad \Delta H_j = F(r, \theta)\gamma_j G_j, \qquad (r, \theta) \in D, \tag{3.18}$$

and

$$G_j = H_j = 0 \quad \text{on} \quad \partial D. \tag{3.19}$$

The above Dirichlet problem consiting of the two coupled Poisson equations (3.18) and boundary conditions (3.19) is solved numerically by the following iterative scheme

$$\Delta \bar{G}_j^{(k+1)} = -F(r, \theta)(\gamma_j H_j^{(k)} + 1), \qquad \Delta \bar{H}_j^{(k+1)} = F(r, \theta)\gamma_j \bar{G}_j^{(k+1)}, \qquad (r, \theta) \in D, \tag{3.20}$$

subject to the boundary conditions

$$\bar{G}_j^{(k+1)} = \bar{H}_j^{(k+1)} = 0 \quad \text{on} \quad \partial D, \tag{3.21}$$

where k refers to the level of iteration. We obtain the updated values of $G_j^{(k+1)}$ and $H_j^{(k+1)}$ for the next level from the intermediate values of $\bar{G}_j^{(k+1)}$ and $\bar{H}_j^{(k+1)}$, using the following relaxation technique

$$G_j^{(k+1)} = \lambda \bar{G}_j^{(k+1)} + (1-\lambda) G_j^{(k)}, \quad H_j^{(k+1)} = \lambda \bar{H}_j^{(k+1)} + (1-\lambda) H_j^{(k)}, \quad \text{in} \quad D, \tag{3.22}$$

where $0 < \lambda \leq 1$ is a relaxation (or smoothing) parameter. The above overall iterative procedure is equivalent to the Gauss-Seidel SOR method. An initial guess $G_0^{(0)}(r,\theta) = H_0^{(0)}(r,\theta) = 0, \ \forall \ (r,\theta) \in D$ starts the iteration procedure. For $j \geq 1$, the converged solution for the previous value of j is used as the initial guess solution. The iteration is continued until the following convergence criterion is met with ϵ as a tolerance parameter:

$$\|G_j^{(k+1)}(r,\theta) - G_j^{(k)}(r,\theta)\|_2 \leq \epsilon, \quad \text{and} \quad \|H_j^{(k+1)}(r,\theta) - H_j^{(k)}(r,\theta)\|_2 \leq \epsilon. \tag{3.23}$$

It is worth mentioning that the initial-guess solution $G_j^{(0)}(r,\theta)$, as well as the smoothing solution $G_j^{(k+1)}(r,\theta), \ k \geq 1$, obtained from Equation (3.22), are not really used in the above iterative scheme. However, these are used in the convergence criterion (3.23).

The above numerical scheme requires solving two Poisson equations in each iteration for each j. Therefore we need to solve approximately $2KL$ Poisson equations, where K is the number of Fourier coefficients used for numerical purposes and L is the average number of iterations required for each j in the above iteration. Since this could be expensive numerically, in particular if K and/or L are large, we adapt a recently developed fast algorithm for the Poisson equation in a circular disk [22] to our annular region with appropriate modification. We discuss this algorithm next.

4. A fast algorithm for the Poisson equation in an annular disk

In this section, we present a fast algorithm for the Poisson equation in an annular disk with Dirichlet boundary condition which is used to solve the iteration scheme (3.20) and (3.21). Various fast algorithms to solve elliptic equations exist, but here we use the one originally developed by Daripa and co-workers [22, 23, 24] for this kind of problem. In [22] a fast algorithm is presented to solve the Poisson equation in a circular disk with Dirichlet and Neumann boundary conditions. Here that algorithm is modified suitably to extend it to an annular disk. We consider the problem

$$\left.\begin{array}{ll} \Delta w = f(r,\theta) & \text{in} \ \ D \\ w = g(\theta) & \text{on} \ \ \partial D \end{array}\right\}, \tag{4.1}$$

where $D = \{\xi \in \mathbb{R}^2 : \ /\beta_1 < |\xi| < \beta_2\}$ and $\partial D = \{\xi \in \mathbb{R}^2 : \ |\xi| = \beta_1 \text{ or } |\xi| = \beta_2\}$. Let

$$g(\theta) = \begin{cases} g_1(\theta), & \text{if } \xi = \beta_1 e^{i\theta}, \quad \theta \in [0, 2\pi], \\ g_2(\theta), & \text{if } \xi = \beta_2 e^{i\theta}, \quad \theta \in [0, 2\pi]. \end{cases} \tag{4.2}$$

We can express the solution of the problem (4.1) in the form

$$w(r,\theta) = u(r,\theta) + v(r,\theta), \tag{4.3}$$

where $u(r,\theta)$ and $v(r,\theta)$ satisfy,

$$\Delta u = f(r,\theta) \quad \text{in} \quad D, \tag{4.4}$$

and

$$\left.\begin{array}{ll} \Delta v = 0 & \text{in } D \\ v = g - u & \text{on } \partial D \end{array}\right\}, \tag{4.5}$$

respectively. In Subsections 4.1 and 4.2 we present fast algorithms to find solutions of Equation (4.4) and problem (4.5).

4.1. A SOLUTION OF EQUATION (4.4)

A particular solution of Equation (4.4) can be written as

$$u(\xi) = \iint_D f(\eta) G(\xi,\eta)\, \mathrm{d}\eta_1\, \mathrm{d}\eta_2, \quad \xi \in D, \tag{4.6}$$

where

$$G(\xi,\eta) = \frac{1}{2\pi} \log|\xi - \eta|, \tag{4.7}$$

is the free-space Green's function for the Laplacian in the domain D; $\xi = \xi_1 + \mathrm{i}\xi_2$ and $\eta = \eta_1 + \mathrm{i}\eta_2$. For numerical evaluation of the singular integral in Equation (4.6), the annular domain D is divided into a grid formed by a set of radial lines and a set of circular lines concentric with the boundaries $|\xi| = \beta_1$ and $|\xi| = \beta_2$. The use of standard quadrature rules to evaluate the integral in Equation (4.6) leads to poor accuracy. Moreover, the complexity of the quadrature method is $O(N^4)$ for a N^2 grid points in the annular domain D. For large N, the method becomes expensive in terms of computational time. However, the integrals in Equation (4.6) can be computed accurately and rapidly by extending the fast algorithm originally developed by Daripa and collaborators [22, 23, 24] to the annular domain.

The mathematical foundation of the fast algorithm to evaluate the particular solution (4.6) is embedded in the following theorem. Here, we represent the particular solution $u(r,\theta)$ as a Fourier series with radius-dependent Fourier coefficients $u_n(r)$. These Fourier coefficients $u_n(r)$ are obtained in terms of one-dimensional integrals in the radial direction. We will not present the proof of the theorem, since it can be proved easily following the method given in [22] for a circular disk.

Theorem 1. *If $f_n(r)$ is the nth Fourier coefficient of the function $f(r,\theta)$, then the nth Fourier coefficient $u_n(r)$ of the solution $u(r,\theta)$ can be written as*

$$u_n(r) = \int_{\beta_2}^{r} p_n(r,\rho)\mathrm{d}\rho + \int_{r}^{\beta_1} q_n(r,\rho)\mathrm{d}\rho, \tag{4.8}$$

where

$$p_n(r,\rho) = \begin{cases} \rho \log r f_0(\rho), & n = 0, \\ -\dfrac{\rho}{2|n|}\left(\dfrac{\rho}{r}\right)^{|n|} f_n(\rho), & n \neq 0, \end{cases} \tag{4.9}$$

and

$$q_n(r,\rho)=\begin{cases}\rho\log\rho f_0(\rho), & n=0,\\ -\dfrac{\rho}{2|n|}\left(\dfrac{r}{\rho}\right)^{|n|} f_n(\rho), & n\neq 0.\end{cases} \tag{4.10}$$

Despite the fact that the above theorem presents the mathematical foundation of the algorithm, an efficient implementation can be made by devising suitable recursive relations to carry out the one-dimensional integration in Equation (4.8) and to evaluate the Fourier coefficients $u_n(r)$ of the solution $u(r,\theta)$. Let the annular domain $D=\{\xi\in\mathbb{R}^2 : \beta_2\le|\xi|\le\beta_1\}$ be discretized into NxM grid points with N equidistant points in the angular direction and M equidistant points in radial direction. Theorem 1 leads to the following corollary.

Corollary 1. *Let* $\beta_2=r_1<r_2<\cdots<r_M=\beta_1$. *Define*

$$C_n^{i,j}=\begin{cases}\displaystyle\int_{r_i}^{r_j}\frac{\rho}{2n}\left(\frac{r_j}{\rho}\right)^n f_n(\rho)\mathrm{d}\rho, & n<0,\\ \displaystyle\int_{r_i}^{r_j}\rho f_n(\rho)\mathrm{d}\rho, & n=0,\end{cases} \tag{4.11}$$

and

$$D_n^{i,j}=\begin{cases}-\displaystyle\int_{r_i}^{r_j}\frac{\rho}{2n}\left(\frac{r_i}{\rho}\right)^n f_n(\rho)\,\mathrm{d}\rho, & n>0,\\ \displaystyle\int_{r_i}^{r_j}\rho\log\rho f_n(\rho)\mathrm{d}\rho, & n=0.\end{cases} \tag{4.12}$$

Let $r_j>r_i$ *and define*

$$\begin{cases}u_n^-(r_1)=0, & n\le 0,\\ u_n^-(r_j)=\left(\dfrac{r_j}{r_i}\right)^n u_n^-(r_i)+C_n^{i,j}, & n\le 0,\end{cases} \tag{4.13}$$

and

$$\begin{cases}u_n^+(r_M)=0, & n\ge 0,\\ u_n^+(r_i)=\left(\dfrac{r_i}{r_j}\right)^n u_n^+(r_j)+D_n^{i,j}, & n\ge 0.\end{cases} \tag{4.14}$$

Then, for $i=1,2,\ldots,n$, *we have*

$$u_n(r_i)=\begin{cases}u_n^-(r_i)+\overline{u_{-n}^+(r_i)}, & n<0,\\ \log(r_i)u_n^-(r_i)+u_n^+(r_i), & n=0,\\ u_n^+(r_i)+\overline{u_{-n}^-(r_i)}, & n>0.\end{cases} \tag{4.15}$$

The above corollary defines the recursive relations to obtain the Fourier coefficients $u_n(r)$ of the solution $u(r,\theta)$ based on the sign of the index n of u_n. Equation (4.13) constructs $n \le 0$ modes from the smallest radius r_1 towards the largest radius r_M. Conversely, Equation (4.14) constructs $n \ge 0$ modes from r_M to r_1. The steps involved in computing a particular solution $u(r,\theta)$ of Equation (4.4) in an annular region D are presented in Algorithm 1 below.

Algorithm 1: Computation of solutions of Equation (4.4) in the annular domain D.

For given grid size $M \times N$, equidistant grid points ($r_l = \beta_2 + (l-1)(\beta_1 - \beta_2)/(M-1)$, $\theta_k = 2\pi k/N$), and specified grid values $f(r_l e^{i\theta_k})$, the algorithm returns the solution values $u(r_l e^{i\theta_k})$ for $l \in [1, M]$ and $k \in [1, N]$.

1. Compute the Fourier coefficients $f_n(r_l),\ n \in [-N/2, N/2]$, for each $l \in [1, M]$ of the grid data $f(r_l e^{i\theta_k}),\ l \in [1, M],\ k \in [1, N]$, using FFT.
2. For $l \in [1, M-1]$, compute the one-dimensional radial integrals $C_n^{l,l+1},\ n \in [-N/2, 0]$, and $D_n^{l,l+1},\ n \in [0, N/2]$, as defined in Equations (4.11) and (4.12) using the trapezoidal rule.
3. Compute the coefficients $u_n^-(r_l),\ n \in [-N/2, 0],\ l \in [1, M]$, as defined by Equation (4.13):
   (a) Set $u_n^-(r_1) = 0,\ n \in [-N/2, 0]$.
   (b) For $l = 2, \cdots, M$, compute
   $$u_n^-(r_l) = \left(\frac{r_l}{r_{l-1}}\right)^n u_n^-(r_{l-1}) + C_n^{l-1,l},\quad n \in [-N/2, 0].$$
4. Compute the coefficients $u_n^+(r_l),\ n \in [0, N/2],\ l \in [1, M]$, as defined by Equation (4.14):
   (a) Set $u_n^+(r_M) = 0,\ n \in [0, N/2]$.
   (b) For $l = M-1, \cdots, 1$, compute
   $$u_n^+(r_l) = \left(\frac{r_l}{r_{l+1}}\right)^n u_n^+(r_{l+1}) + D_n^{l,l+1},\quad n \in [0, N/2].$$
5. Compute the Fourier coefficients $u_n(r_l),\ n \in [-N/2, N/2],\ l \in [1, M]$, by combining coefficients $u_n^-(r_l)$ and $u_n^+(r_l)$ as in Equation (4.15).
   For $l = 1, 2, \cdots, M$, compute
   $$u_n(r_l) = u_n^-(r_l) + \overline{u_{-n}^+(r_l)}, n \in [-N/2, -1],$$
   $$u_0(r_l) = \log(r_l) u_0^-(r_l) + u_0^+(r_l),$$
   $$u_n(r_l) = \overline{u_{-n}(r_l)},\ n \in [1, N/2].$$
6. Compute the solution values $u(r_l e^{i\theta_k}), l \in [1, M], k \in [1, N]$, from the Fourier coefficients $u_n(r_l), l \in [1, M], n \in [-N/2, N/2]$, using FFT.

4.2. Solution of problem (4.5)

The solution for the harmonic function $v(r,\theta)$ in the annular domain D satisfying the Dirichlet boundary conditions (see Equations (4.5)) can be represented as an infinite series. This solution is available in many elementary books on partial differential equations and/or applied mathematics. Below, for the sake of completeness, we present this solution as a theorem (and also its proof).

Theorem 2. *Let a_n and b_n be the nth Fourier coefficients of the boundary functions $h_1(\theta)$ and $h_2(\theta)$ defined by*

$$h_1(\theta) = g_1(\theta) - u(\beta_1, \theta) \quad \text{and} \quad h_2(\theta) = g_2(\theta) - u(\beta_2, \theta). \tag{4.16}$$

Then the Fourier coefficients $v_n(r)$ of the solution $v(r, \theta)$ of (4.5) are given by

$$v_n(r) = \begin{cases} C_0 \log r + D_0, & \text{if } n = 0, \\ C_n r^{-n} + D_n r^n, & \text{if } n \neq 0, \end{cases} \tag{4.17}$$

where

$$C_0 = \frac{a_0 - b_0}{\log(\beta_1/\beta_2)} \quad \textit{and} \quad D_0 = \frac{b_0 \log \beta_1 - a_0 \log \beta_2}{\log(\beta_1/\beta_2)}, \tag{4.18}$$

and

$$C_n = \frac{\beta_1^n \beta_2^n (b_n \beta_1^n - a_n \beta_2^n)}{(\beta_1^{2n} - \beta_2^{2n})} \quad \textit{and} \quad D_n = \frac{(a_n \beta_1^n - b_n \beta_2^n)}{(\beta_1^{2n} - \beta_2^{2n})}. \tag{4.19}$$

Proof. If we represent the solution $v(r, \theta)$ of problem (4.5) by the Fourier series

$$v(r, \theta) = \sum_{n=-\infty}^{\infty} v_n(r) \mathrm{e}^{\mathrm{i}n\theta}, \tag{4.20}$$

then the Fourier coefficients $v_n(r)$ satisfy Euler's differential equation

$$\frac{\mathrm{d}^2 v_n}{\mathrm{d}r^2} + \frac{1}{r}\frac{\mathrm{d}v_n}{\mathrm{d}r} - \frac{n^2}{r^2} v_n = 0, \tag{4.21}$$

and the boundary conditions

$$v_n(r = \beta_1) = a_n \quad \text{and} \quad v_n(r = \beta_2) = b_n. \tag{4.22}$$

Now it is easy to see that the $v_n(r)$ described by Equations (4.17)–(4.19) satisfy the boundary-value problem (4.21) and (4.22). This completes the proof of the Theorem 2.

Note: It can be easily shown that $C_n = \overline{D_{-n}}$.

Algorithm 2: Computation of the solution of Equation (4.5) in the annular domain D.
For given grid size $M \times N$, the equidistant grid points ($r_l = \beta_2 + (l-1)(\beta_1 - \beta_2)/(M-1)$, $\theta_k = 2\pi k/N$), and given boundary values $h_1(\theta_k)$ and $h_2(\theta_k)$, the algorithm returns the solution values $v(r_l \mathrm{e}^{\mathrm{i}\theta_k})$, $l \in [1, M]$, $k \in [1, N]$.

1. Compute the Fourier coefficients a_n and b_n, $n \in [-N/2, N/2]$, of the boundary data $h_1(\theta_k)$ and $h_2(\theta_k)$, $k \in [1, N]$, using FFT.

2. Compute the coefficients C_n and D_n, $n \in [-N/2, N/2]$, using Equations (4.18) and (4.19).

3. Compute the Fourier coefficients $v_n(r_l)$, $n \in [-N/2, N/2]$, $l \in [1, M]$, for the solution $v(r, \theta)$ using Equation (4.17).

4. Compute the solution values $v(r_l \mathrm{e}^{\mathrm{i}\theta_k})$, $l \in [1, M]$, $k \in [1, N]$, from the Fourier coefficients $v_n(r_l)$, $l \in [1, M]$, $n \in [-N/2, N/2]$, using FFT.

Finally, we add the solutions obtained from Algorithm-1 for Equation (4.4) and from Algorithm-2 for problem (4.5) to obtain the desired solution of problem (4.1).

4.3. THE ALGORITHMIC COMPLEXITY

Here we consider the computational complexity of the above algorithm. In steps 1 and 5 of Algorithm-1, there are 2M FFT's of length N and all other computations in steps 2, 3 and 4 are of lower order. Similarly, in steps 1 and 4 of Algorithm-2, there are 2M FFT's of length N and all other computations in steps 2 and 3 are of lower order. With each FFT of length N contributing $N \log N$ operations, the asymptotic operation count and hence the asymptotic time complexity is $O(MN \log N)$. It is easy to see that the asymptotic storage requirement is of the order $O(MN)$. Finally, we remark that the above algorithms are both very parallelizable on multi-processor machines (see [22] for details).

5. Numerical results and discussions

The objective of the present study is to apply an iterative technique and an efficient fast algorithm to compute accurately and rapidly the flow characteristics corresponding to the pulsatile flow of blood in an eccentric catheterized artery. The fast algorithm basically solves the Poisson equation in an annular domain with Dirichlet conditions on the boundaries. In fact, it is a modified version of the fast algorithm of Borges and Daripa [22] developed originally for the Poisson equation in a circular disk with Dirichlet and Neumann conditions on the boundary.

The flow modeling involves the usual assumptions that (i) the arterial segment is straight, (ii) the arterial wall is rigid and impermeable, (iii) the artery and the catheter are infinitely long and the pressure-sensing device is mounted on the catheter at a large distance upstream from the tip of the catheter, (iv) blood is an incompressible Newtonian fluid, and (v) the flow is fully developed. The flux (flow rate) $Q(t)$ is considered to be a prescribed periodic function of time t. With these assumptions and conditions, numerical results for the axial pressure gradient $\frac{\partial p}{\partial z}(t)$ and velocity distribution $w(x, y, t)$ in the eccentric catheterized artery are obtained for several values of the Womersley frequency parameter α, the radii ratio a, and the eccentricity parameter c. These results are used to obtain the estimates of the increased mean pressure gradient and frictional resistance in the artery due to the insertion of a catheter into it. The above - mentioned results and estimates in a concentric catheterized artery (*i.e.*, when $c = 0$) are also obtained in this paper based on the analysis presented in the Appendix.

The model problem in the Fourier space reduces to solving two coupled Poisson Equations (3.18) with Dirichlet boundary conditions (3.19), for each Fourier mode $j \in [-K, K]$, where K is the number of harmonics in the Fourier series representation of the prescribed periodic flow rate $Q(t)$ (see below in (5.1) the representation of $Q(t)$ for which K is 6). These Dirichlet problems are solved numerically by means of the iterative scheme (3.20) and (3.21), smoothing technique (3.22), and convergence criterion (3.23). The corresponding iterative scheme in the case of zero eccentricity is given by Equations (A7) and (A8). Numerical experiments are performed with the error tolerance ϵ in (3.23) set at 10^{-7}, the number of grid points in the radial direction $(M + 1)$ set at 101, and the number of grid points in the angular direction (N) set at 128. The values of the radii ratio a and the eccentricity parameter c are chosen to satisfy $a < 1$, $c \geq 0$ and $a + c < 1$. The values of the Womersley frequency

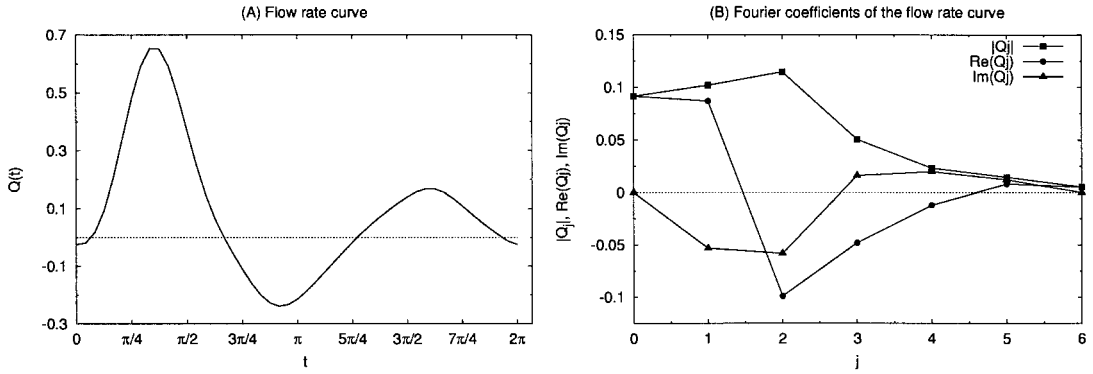

Figure 2. (A) Time variation of flow rate $Q(t)$ during a cycle of oscillation. (B) Behavior of the Fourier coefficients Q_j of the flow rate $Q(t)$.

Table 1. The amplitudes and moduli of the harmonics of the flow rate $Q(t)$ which is defined by Equation (5.1) and shown in Figure 2(A).

j	0	1	2	3	4	5	6
Q_j^*	0·0916	0·2040	0·2292	0·1011	0·0464	0·0291	0·0106
ψ_j	0·0	0·5482	2·6100	3·4670	4·1670	5·3035	6·2832

parameter α are chosen up to 3·5, the value $\alpha \approx 3{\cdot}35$ being suitable for a canine femoral artery as well as for a coronary artery [12, 25].

It is found that the convergence of the overall iterative scheme (3.20)–(3.23) depends largely on the values of the Womersley frequency parameter α, radii ratio a, and eccentricity parameter c. Based on our numerical experiments with the smoothing or relaxation parameter λ fixed at $\lambda = 1$ (*i.e.*, Gauss-Seidel type of iteration technique without smoothing), we have made the following observations regarding the convergence of the iterative scheme for Fourier modes $j \in [-6, 6]$. (i) For $\alpha \leq 1$, the scheme converges for almost all values of a and c in the range given above. (ii) For higher values of a (*e.g.*, $a = 0{\cdot}75$) and lower values of c (*e.g.*, $c = 0{\cdot}15$), the scheme converges for higher values of α (*e.g.*, $\alpha \leq 3$). (iii) Finally, as the value of a decreases and c increases, the scheme converges for relatively lower values of α.

To achieve the convergence of the scheme for all $j \in [-6, 6]$ and all physically realistic values of α, a and c, we use the smoothing technique (3.22) with a suitably chosen smoothing parameter $0 < \lambda \leq 1$. The choice of λ exerts a control over the convergence of the overall iterative scheme (3.20)–(3.23) in the sense that, if the scheme tends to diverge for a given value of λ, the gradual reduction in the value of λ eventually brings out convergence. So, the choice of λ depends largely on the values of the parameters α, a and c. We have observed that the value of λ for which the scheme converges decreases as the value of α or c increases or the value of a decreases. It was difficult to find a single optimum value of λ for which the scheme converges very rapidly for all $j \in [-6, 6]$ and for all values of α, a and c.

Figure 2(A) shows the plot of $Q(t)$ versus t during a cycle of oscillation that is used to compute the axial pressure gradient $\partial p/\partial z(t)$ and velocity distribution $w(x, y, t)$ in the eccentric catheterized artery for several values of the Womersley frequency parameter α, the

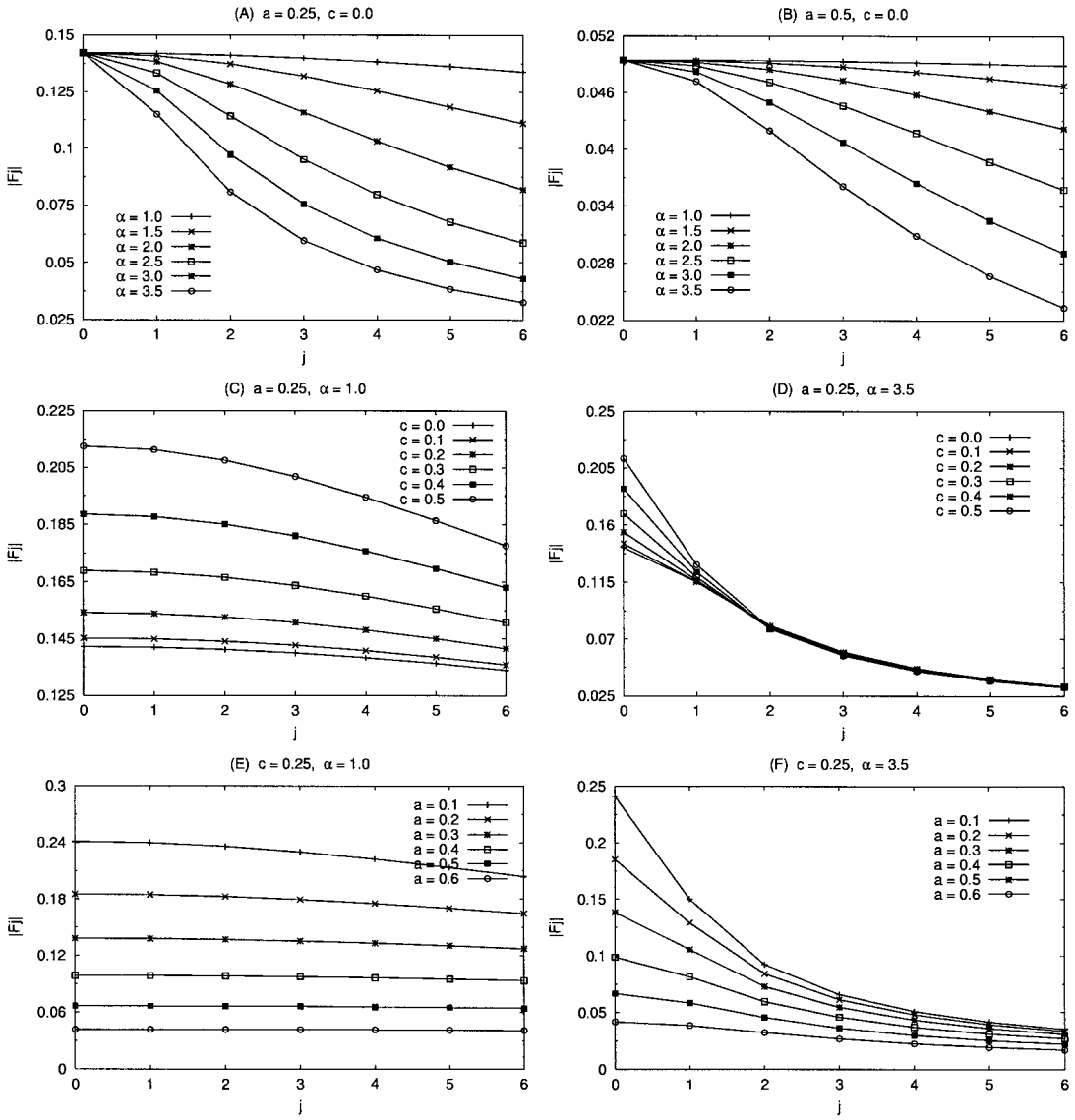

Figure 3. Plots of $|F_j|$ *vs.* j; plots in (A) and (B) are for several values of α with (A) $a = 0{\cdot}25, c = 0$ and (B) $a = 0{\cdot}5, c = 0$; plots in (C) and (D) are for several values of c with (C) $a = 0{\cdot}25, \alpha = 1$ and (D) $a = 0{\cdot}25, \alpha = 3{\cdot}5$; plots in (E) and (F) are for several values of a with (E) $c = 0{\cdot}25, \alpha = 1$ and (F) $c = 0{\cdot}25, \alpha = 3{\cdot}5$.

radii ratio a, and the eccentricity parameter c. This plot represents an approximation to the measured flow rate (flux) in a canine femoral artery [12, 25]. It is specified by the equation

$$Q(t) = \sum_{j=0}^{6} Q_j^* \cos(jt - \psi_j), \tag{5.1}$$

where Q_j^* and ψ_j, $j = 0, 1, \ldots, 6$, are the amplitudes and moduli of the harmonics of the flow rate $Q(t)$ which are specified in Table 1. The series (5.1) can be written in the form of complex Fourier series (2.7) if we define

$$Q_0 = Q_0^* \cos(\psi_0), \quad Q_j = \tfrac{1}{2} Q_j^* \mathrm{e}^{-\mathrm{i}\psi_j}, \quad \text{and} \quad Q_{-j} = \overline{Q_j}, \quad j > 0. \tag{5.2}$$

The magnitude, real, and imaginary parts of the Fourier coefficients Q_j for $0 \leq j \leq 6$ are plotted in Figure 2(B). The Fourier coefficients Q_j for $|j| > 6$ are set to zero.

The behavior of the computed solutions E_j of the Dirichlet problem (3.12) and (3.13), when $c > 0$ and boundary-value problem (A3) and (A4) when $c = 0$, are described through various plots in Figure 3. It shows the plots of $|F_j|$ *vs.* j for several values of Womersley frequency parameter α in Figures 3(A) and 3(B) with (A) $a = 0{\cdot}25, c = 0$ and (B) $a = 0{\cdot}5, c = 0$; for several values of eccentricity parameter c in Figures 3(C) and 3(D) with (C) $a = 0{\cdot}25, \alpha = 1$ and (D) $a = 0{\cdot}25, \alpha = 3{\cdot}5$; and for several values of radii ratio a in Figures 3(E) and 3(F) with (E) $c = 0{\cdot}25, \alpha = 1$ and (F) $c = 0{\cdot}25, \alpha = 3{\cdot}5$. Here the variables F_j's are related to the functions E_j's by

$$F_j = \begin{cases} 2\pi \displaystyle\int_a^1 E_j(r) r \,\mathrm{d}r, & \text{if} \quad c = 0, \\ \displaystyle\int_0^{2\pi} \int_{\beta_2}^{\beta_1} F(r,\theta) E_j(r,\theta) r \,\mathrm{d}r \mathrm{d}\theta, & \text{if} \quad c > 0. \end{cases} \tag{5.3}$$

In fact, F_j represents the denominator in Equations (3.16) and (A12). From the various plots in Figure 3, it is seen that (i) $|F_j|$ decreases with increasing j (*i.e.*, $\partial|F_j|/\partial j < 0$). However, the $|F_j|$'s are almost independent of j for lower values of α and c and higher values of a. (ii) $|F_j|$ decreases with the increasing value of α (*i.e.*, $\partial|F_j|/\partial\alpha < 0$). Also, the variation of $|F_j|$ with α is quite large for lower values of a and higher values of c and j; the zeroth mode $|F_0|$ is independent of α. (iii) $|F_j|$ increases with increasing value of c (*i.e.*, $\partial|F_j|/\partial c > 0$) for smaller values of α. Also, the $|F_j|$'s for $j \geq 2$ are almost independent of c for higher values of α, as shown in Figure 3(D) with $\alpha = 3{\cdot}5$. (iv) Finally, $|F_j|$ decreases with the increasing value of a (*i.e.*, $\partial|F_j|/\partial a < 0$). The case (iv) is consistent with the fact that the cross-sectional area of the catheterized artery decreases with an increase in the radii ratio a.

The behavior of the Fourier coefficients P_j of the axial pressure gradient $\partial p/\partial z(t)$, computed from Equation (3.16), is described by Figure 4. It shows the plots of $|P_j|$ *vs.* j for several values of the Womersley frequency parameter α in Figures 4(A) and 4(B) with (A) $a = 0{\cdot}25, c = 0$ and (B) $a = 0{\cdot}5, c = 0$; for several values of eccentricity parameter c in Figures 4(C) and 4(D) with (C) $a = 0{\cdot}25, \alpha = 1$ and (D) $a = 0{\cdot}25, \alpha = 3{\cdot}5$; and for several values of radii ratio a in Figures 4(E) and 4(F) with (E) $c = 0{\cdot}25, \alpha = 1$ and (F) $c = 0{\cdot}25, \alpha = 3{\cdot}5$. The time variation of the corresponding axial pressure gradient $\partial p/\partial z(t)$, as computed from Equation (3.1), during a cycle of oscillation is plotted in Figure 5.

It is seen from Figure 4 that $|P_j|$ decays very rapidly for $j > 2$. Also, $|P_0|$ is independent of the Womersley frequency parameter α. In fact, the zeroth Fourier mode P_0 corresponds to the desired pressure gradient in a catheterized artery in steady-state flow conditions. The other modes account for the unsteady (pulsatile) state of the flow. It is again seen from Figure 4 that $|P_j|$ increases with increasing values of α and a, but decreases with increasing values of c. Also, the $|P_j|$s vary considerably with α and a, but not with c. In fact, for higher values of α (*e.g.*, $\alpha = 3{\cdot}5$), the $|P_j|$s are almost independent of c for $j > 2$, as seen in Figure 4(D).

Figure 5 gives a complete description of the axial pressure gradient $\partial p/\partial z(t)$ in a catheterized artery for almost all physically as well as physiologically realistic values of Womersley frequency parameter α, radii ratio a, and eccentricity parameter c. This includes results for a concentric catheterized artery too. Actually, this is the amount of pressure gradient required

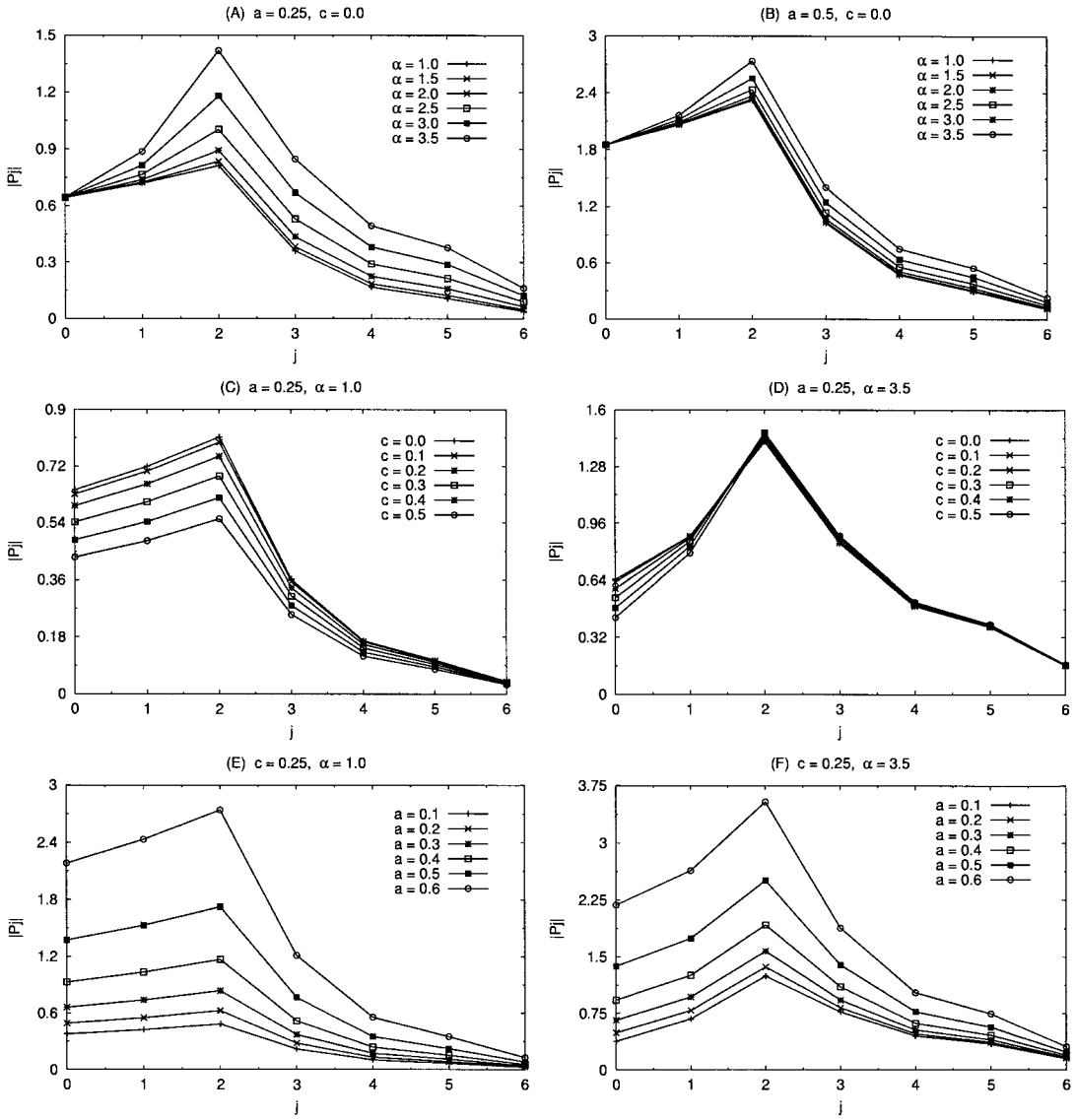

Figure 4. Plots of $|P_j|$ *vs.* j; plots in (A) and (B) are for several values of α with (A) $a = 0{\cdot}25, c = 0$ and (B) $a = 0{\cdot}5, c = 0$; plots in (C) and (D) are for several values of c with (C) $a = 0{\cdot}25, \alpha = 1$ and (D) $a = 0{\cdot}25, \alpha = 3{\cdot}5$; plots in (E) and (F) are for several values of a with (E) $c = 0{\cdot}25, \alpha = 1$ and (F) $c = 0{\cdot}25, \alpha = 3{\cdot}5$.

in the catheterized artery for generating the prescribed mass-flow rate (flux). Therefore, this is the elevated pressure gradient in the artery due to the insertion of a catheter into it. We can estimate the amount of increased pressure gradient from Figure 5.

We can infer the following regarding the dependence of $\partial p/\partial z(t)$ on the values of α, a and c from the various plots in Figure 5: (i) Unlike the prescribed mass flux $Q(t)$, the axial pressure gradient $\partial p/\partial z(t)$ varies considerably during a cycle of oscillation. (ii) $\partial p/\partial z(t)$ depends strongly on α and a, but only weakly on c. To exemplify this, consider some results in a concentric catheterized artery shown in Figures 5(A) and 5(B). When the value of a is $0{\cdot}25$, the maximum value of $\partial p/\partial z(t)$ is approximately $4{\cdot}7$ for $\alpha = 1$ and $8{\cdot}4$ for $\alpha = 3{\cdot}5$.

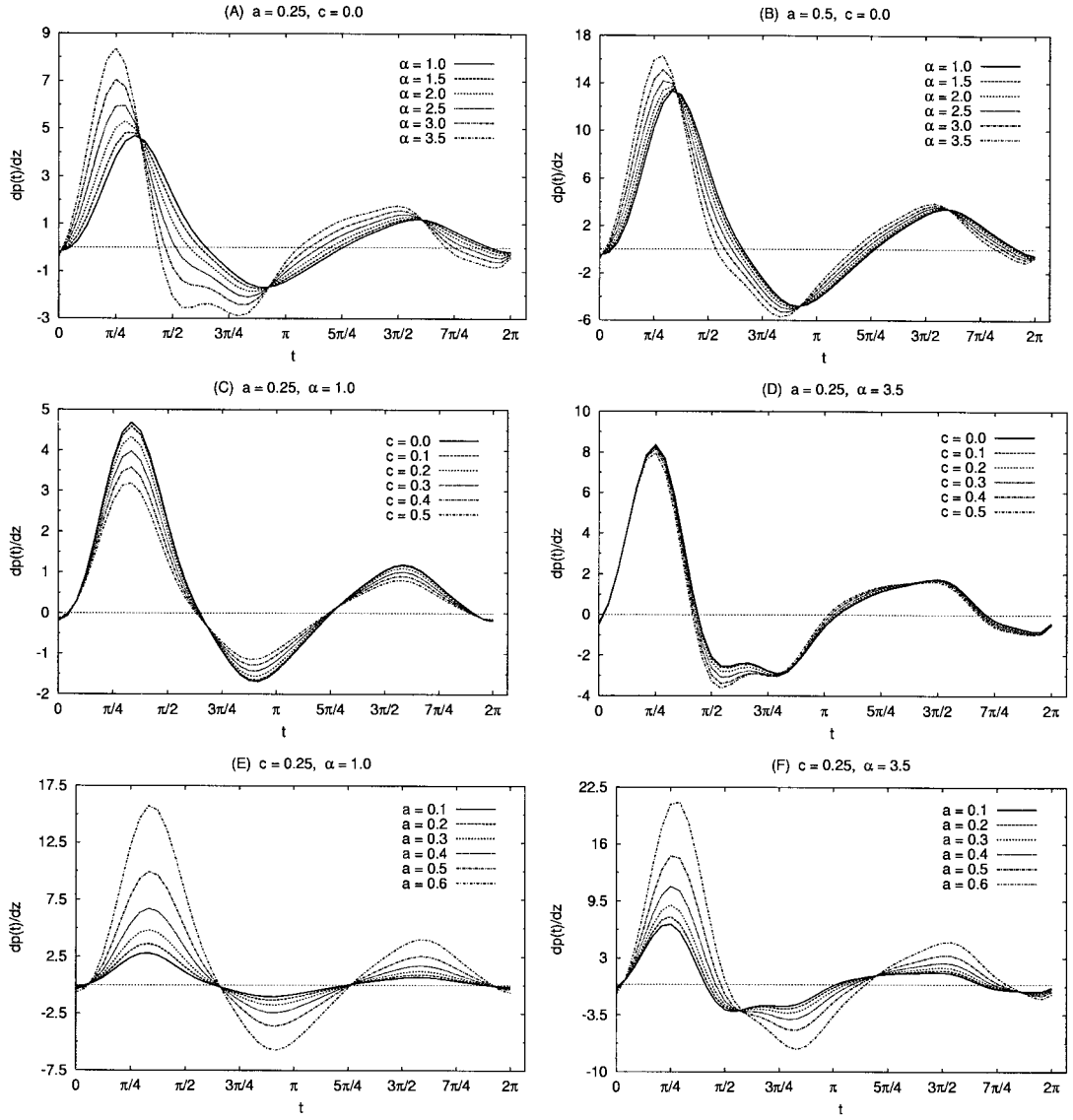

Figure 5. Time variation of the axial pressure gradient $\frac{\partial p}{\partial z}(t)$ during a cycle of oscillation; plots in (A) and (B) are for several values of α with (A) $a = 0{\cdot}25, c = 0$ and (B) $a = 0{\cdot}5, c = 0$; plots in (C) and (D) are for several values of c with (C) $a = 0{\cdot}25, \alpha = 1$ and (D) $a = 0{\cdot}25, \alpha = 3{\cdot}5$; plots in (E) and (F) are for several values of a with (E) $c = 0{\cdot}25, \alpha = 1$ and (F) $c = 0{\cdot}25, \alpha = 3{\cdot}5$.

But, as the value of a increases to 0·5, the maximum value becomes 13·3 for $\alpha = 1$ and 16·3 for $\alpha = 3{\cdot}5$. So, the maximum value of $\partial p/\partial z(t)$ over the duration of a cycle depends strongly on α and a. (iii) For smaller values of α, $\partial p/\partial z(t)$ varies smoothly during a cycle of oscillation for almost all values of a and c and, therefore, shows the qualitative behavior of the prescribed mass-flow rate $Q(t)$. In these cases, the inertial effects are not significant. However, as the value of α increases, the curves tend to become irregular for lower values of a and higher values of c due to the increased inertial effects. (iv) It is seen from Figures 5(A) and 5(B) that the time at which $\partial p/\partial z(t)$ attains its maximum during a cycle of oscillation

Table 2. The mean (time-averaged over a cycle of oscillation) axial pressure gradient $\partial\tilde{p}/\partial z$ in the catheterized artery as a function of radii ratio a and eccentricity parameter c. The mean flow rate is $Q_0 = Q_0^* \cos(\psi_0) = Q_0^* = 0{\cdot}0916$.

$c\backslash a$	0·1	0·2	0·3	0·4	0·5	0·6	0·7
0·0	0·406	0·548	0·767	1·142	1·852	3·403	7·607
0·1	0·402	0·538	0·748	1·100	1·753	3·120	6·538
0·2	0·389	0·512	0·696	0·994	1·513	2·503	4·610
0·3	0·368	0·474	0·625	0·858	1·237	1·892	–
0·4	0·347	0·432	0·550	0·725	0·992	–	–
0·5	0·323	0·389	0·480	0·609	–	–	–
0·6	0·300	0·351	0·420	–	–	–	–

decreases with increasing values of α. Thus, the moduli (phase shift) of various harmonics of the axial pressure gradient $\partial p/\partial z(t)$ vary with the Womersley frequency parameter α. These moduli are almost independent of the radii ratio a and eccentricity parameter c for lower values of α, but vary with a and c for higher values of α. These results are in good qualitative and quantitative agreement with the results of MacDonald [12], in particular with the Figures 2(B) and 3(A,B) of MacDonald [12].

The time-averaged mean axial pressure gradient $\partial\tilde{p}/\partial z$ in a catheterized artery obtained as a function of radii ratio a and eccentricity parameter c is presented in Table 2. Since $\partial\tilde{p}/\partial z$ is equal to the zeroth Fourier mode P_0 of $\partial p/\partial z(t)$, these results are independent of the Womersley frequency parameter α. The entries missing in this table correspond to inadmissible values of the pair (a, c) for which computation has not been done, as these are physically meaningless. The time-averaged mean flow rate $\tilde{Q}$ obtained from Equation (5.1) is 0·0916. The mean frictional resistance is calculated from these values as the ratio of the mean pressure gradient to mean flow rate. So, this table basically indicates how the mean axial pressure gradient and frictional resistance will vary with the radii ratio a and eccentricity parameter c when a catheter is inserted into the artery. It is seen that $\partial\tilde{p}/\partial z$ increases with an increase in the values of a, but decreases with an increase in the values of c, the variation with a being quite high as compared to that with c. From this table, the factor by which the mean pressure gradient, or equivalently, the mean frictional resistance increases due to catheterization can be calculated.

Figure 6 shows the velocity profiles on the x-axis at various time levels during a cycle of oscillation with $a = 0{\cdot}2$ and $c = 0{\cdot}3$. The plots in Figure 6(A) show $w(x, y, t)$ *vs.* x when $x \in [c + a, 1]$, $y = 0$, and $t = 0, \pi/4, \cdots, 7\pi/4$, and the plots in Figure 6(B) show $w(x, y, t)$ *vs.* x when $x \in [-1, c - a]$, $y = 0$, and $t = 0, \pi/4, \cdots, 7\pi/4$. These figures clearly show that the velocity profile is skewed towards the inner boundary of the eccentric annulus; the skewness being more prominent when $x \in [-1, c - a]$ as seen in Figure 6(B). The skewed shape of the profile is perhaps due to the greater shear force acting on the fluid near the outer boundary of the eccentric annulus. The velocity profile also shows the behavior of the boundary layer at certain times during the cycle of oscillation.

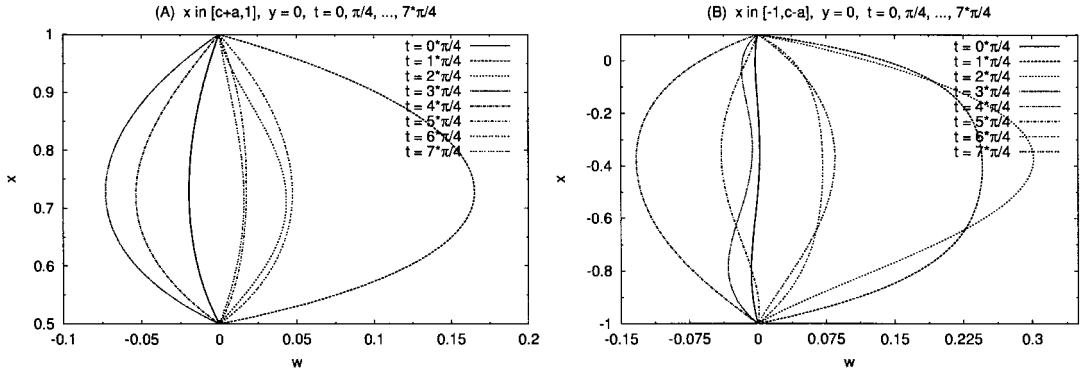

Figure 6. Axial velocity distribution $w(x, y, t)$ on x-axis ($y = 0$) at time $t = 0, \pi/4, \cdots, 7\pi/4$, with $a = 0{\cdot}2$ and $c = 0{\cdot}3$; (A) $x \in [c + a, 1]$ and (B) $x \in [-1, c - a]$.

6. Concluding remarks

The fast algorithm of Borges and Daripa [22] for Dirichlet problems in a circular disk has been extended here for solving Dirichlet problems in an annular disk. This fast algorithm has been implemented and applied to study pulsatile (oscillatory) blood flow in a straight eccentric catheterized artery by modeling blood as an incompressible Newtonian fluid. The axial pressure gradient $\partial p/\partial z(t)$ and velocity distributions $w(x, y, t)$ in the catheterized artery have been obtained as solutions of the problem by prescribing the flow rate $Q(t)$ as a suitable periodic function of time t typical of that of a canine femoral artery. Numerical results have been obtained for various values of the Womersley frequency parameter α, radii ratio a (normalized catheter radius), and eccentricity parameter c (normalized distance between the center of the catheter and the center of the artery). From these numerical results, changes in the mean pressure gradient and frictional resistance due to the insertion of a catheter into an artery have been estimated. These estimates can be used to correct the error involved in the measured pressure gradients using catheters.

The present study shows that the axial pressure gradient $\partial p/\partial z(t)$ in the catheterized artery varies significantly with the Womersley frequency parameter α and radii ratio a. However, it does not vary considerably with the eccentricity parameter c for higher values of the Womersley frequency parameter α. Also, the mean axial pressure gradient as well as mean frictional resistance increases with the increasing catheter radius, but decreases with the increasing distance between the center of the catheter and the center of the artery.

Acknowledgment

The authors are grateful to the referees for their useful comments and suggestions. This material is based in part upon work supported by the Texas Advanced Research Program under Grant No. TARP-97010366-030.

Appendix: The case of zero eccentricity

The case of zero eccentricity (*i.e.*, $c = 0$) can not be derived from our analysis since the conformal mapping (3.8) breaks down as $c \to 0$. Therefore, it has to be treated separately

which is done in this appendix. In the case of $c = 0$, it is convenient to use polar co-ordinates (r, θ, z) to formulate and analyze the problem. Since the flow becomes axially symmetric (*i.e.*, $\frac{\partial}{\partial\theta}() = 0$), the Navier-Stokes equation and the no-slip boundary conditions, in non-dimensional form, are reduced to

$$\alpha^2 \frac{\partial w}{\partial t} = \frac{\partial p}{\partial z} + \frac{\partial^2 w}{\partial r^2} + \frac{1}{r}\frac{\partial w}{\partial r} \quad \text{for} \quad a \le r \le 1, \tag{A1}$$

and

$$w = 0 \quad \text{at} \quad r = a \quad \text{and} \quad r = 1. \tag{A2}$$

So, if the flow rate $Q(t)$ is given by Equation (2.7), then the pressure gradient $\partial p/\partial z(t)$ and the velocity distribution $w(r, t)$ can be expressed in the form of the Fourier series (3.1). Here the Fourier coefficients w_j are functions of r only. The above Dirichlet problem then reduces to the following boundary-value problem (BVP) for an ordinary differential equation.

$$\frac{\mathrm{d}^2 E_j}{\mathrm{d}r^2} + \frac{1}{r}\frac{\mathrm{d}E_j}{\mathrm{d}r} = \mathrm{i}\gamma_j E_j - 1 \quad \text{for} \quad a \le r \le 1 \tag{A3}$$

and

$$E_j = 0 \quad \text{at} \quad r = a \quad \text{and} \quad r = 1, \tag{A4}$$

for $j = 0, \pm1, \pm2, \cdots, \pm\infty$. Here $E_j(r) = w_j(r)/P_j$ and $\gamma_j = j\alpha^2$. An iterative numerical scheme for solving the BVP (A3) and (A4) analogous to the scheme (3.20) and (3.21) can be written as

$$\begin{aligned}
&\left(\frac{\mathrm{d}^2}{\mathrm{d}r^2} + \frac{1}{r}\frac{\mathrm{d}}{\mathrm{d}r}\right) G_j^{(k+1)} = -(\gamma_j H_j^{(k)} + 1), \quad a \le r \le 1, \\
&\left(\frac{\mathrm{d}^2}{\mathrm{d}r^2} + \frac{1}{r}\frac{\mathrm{d}}{\mathrm{d}r}\right) H_j^{(k+1)} = \gamma_j G_j^{(k+1)}, \quad a \le r \le 1,
\end{aligned} \tag{A5}$$

subject to the conditions

$$G_j^{(k+1)} = H_j^{(k+1)} = 0, \quad \text{at} \quad r = a \quad \text{and} \quad r = 1, \tag{A6}$$

where G_j and H_j are the real and imaginary parts of the coefficient E_j. In integral form, the above iterative numerical scheme can be written as

$$\begin{aligned}
G_j^{(k+1)}(r) = &\left[C_j^{(k+1)} - \int_a^r \left(\gamma_j H_j^{(k)} + 1\right)\rho \mathrm{d}\rho\right]\log r \\
&-\left[\int_r^1 \rho \log\rho\left(\gamma_j H_j^{(k)} + 1\right)\mathrm{d}\rho\right], \quad a \le r \le 1, \\
H_j^{(k+1)}(r) = &\left[D_j^{(k+1)} + \gamma_j \int_a^r G_j^{(k+1)}\rho \mathrm{d}\rho\right]\log r \\
&+\left[\gamma_j \int_r^1 \rho \log\rho G_j^{(k+1)}\mathrm{d}\rho\right], \quad a \le r \le 1,
\end{aligned} \tag{A7}$$

where the constants of integration $C_j^{(k+1)}$ and $D_j^{(k+1)}$ are given by

$$C_j^{(k+1)} = \frac{1}{\log a}\int_a^1 \rho \log \rho\big(\gamma_j H_j^{(k)} + 1\big)\mathrm{d}\rho \quad \text{and} \quad D_j^{(k+1)} = -\frac{\gamma_j}{\log a}\int_a^1 \rho \log \rho G_j^{(k)}\mathrm{d}\rho. \tag{A8}$$

In conjunction with the smoothing technique (3.22) (which treats left side of Equation (A7) as intermediate values in Equation (3.22)) and convergence criterion (3.23), the iterative scheme (A7) is used to solve for $G_j(r)$ and $H_j(r)$ and hence $E_j(r)$ for $a < r < 1$.

We have also found the exact analytic solution of the BVP (A3) and (A4) in terms of Bessel functions with complex arguments. For the sake of completeness, we will present these below. However, we have not done any computation with these exact solutions because of the peculiar complex argument of the Bessel functions. Rather, we have found the above iterative scheme more suitable for the computation of the solutions. The analytic solutions for the E_js are given by

$$E_j = \frac{1}{\mathrm{i}\gamma_j}\Big[1 - A_j J_0(\mathrm{i}^{3/2}\gamma_j^{1/2} r) - B_j Y_0(\mathrm{i}^{3/2}\gamma_j^{1/2} r)\Big], \tag{A9}$$

where the constants of integration A_j and B_j are given by

$$A_j = \frac{\Big[Y_0(\mathrm{i}^{3/2}\gamma_j^{1/2}) - Y_0(\mathrm{i}^{3/2}\gamma_j^{1/2} a)\Big]}{\Big[J_0(\mathrm{i}^{3/2}\gamma_j^{1/2} a)Y_0(\mathrm{i}^{3/2}\gamma_j^{1/2}) - J_0(\mathrm{i}^{3/2}\gamma_j^{1/2})Y_0(\mathrm{i}^{3/2}\gamma_j^{1/2} a)\Big]}, \tag{A10}$$

$$B_j = \frac{\Big[J_0(\mathrm{i}^{3/2}\gamma_j^{1/2}) - J_0(\mathrm{i}^{3/2}\gamma_j^{1/2} a)\Big]}{\Big[J_0(\mathrm{i}^{3/2}\gamma_j^{1/2} a)Y_0(\mathrm{i}^{3/2}\gamma_j^{1/2}) - J_0(\mathrm{i}^{3/2}\gamma_j^{1/2})Y_0(\mathrm{i}^{3/2}\gamma_j^{1/2} a)\Big]}. \tag{A11}$$

With the help of the prescribed flux given by Equation (2.7), the Fourier coefficients P_j of the axial pressure gradient $\partial p/\partial z(t)$ can be written as

$$P_j = Q_j \Big/ 2\pi \int_a^1 E_j(r) r \mathrm{d}r, \tag{A12}$$

where

$$\begin{aligned}\int_a^1 E_j r\mathrm{d}r = \frac{1}{\mathrm{i}\gamma_j}\Bigg[\frac{1-a^2}{2} - \frac{A_j}{\mathrm{i}^{3/2}\gamma_j^{1/2}}\Big[J_1(\mathrm{i}^{3/2}\gamma_j^{1/2}) - aJ_1(\mathrm{i}^{3/2}\gamma_j^{1/2} a)\Big] \\ - \frac{B_j}{\mathrm{i}^{3/2}\gamma_j^{1/2}}\Big[Y_1(\mathrm{i}^{3/2}\gamma_j^{1/2}) - aY_1(\mathrm{i}^{3/2}\gamma_j^{1/2} a)\Big]\Bigg].\end{aligned} \tag{A13}$$

References

1. H.V. Anderson, G.S. Roubin, P.P. Leimgruber, W.R. Cox, J.S. Douglas Jr., S.B. King and A.R. Gruentzig, Measurement of transstenotic pressure gradient during percutaneous transluminal coronary angioplasty. *Circulation* 73 (1986) 1223–1230.
2. L.H. Back, Estimated mean flow resistance increase during coronary artery catheterization. *J. Biomech.* 27 (1994) 169–175.

3. L.H. Back, E.Y. Kwack and M.R. Back, Flow rate-pressure drop relation in coronary angioplasty: catheter obstruction effect. *J. Biomech. Engng., Trans. ASME* 118 (1996) 83–89.
4. M.R. Back, R.A. White, E.Y. Kwack and L.H. Back, Hemodynamic consequences of stenosis remodeling during coronary angioplasty. *Angiology* 48 (1997) 99–109.
5. P. Ganz, R. Abben, P.L. Friedman, J.D. Garnic, W.H. Barry and D.C. Levin, Usefulness of transstenotic coronary pressure gradient measurements during diagnostic catheterization. *Am. J. Cardiol.* 55 (1985) 910–914.
6. R.F. Wilson, M.R. Johnson, M.L. Marcus, P.E.G. Aylward, D.J. Skorton, S. Collings and C.W. White, The effect of coronary angioplasty on coronary flow reserve. *Circulation* 77 (1988) 873–885.
7. L. Bjorno and H. Pettersson, Hydro- and hemodynamic effects of catheterization of vessels: I. An experimental model. *Acta Radiol. Diagnosis* 17 (1976) 511–525.
8. L. Bjorno and H. Pettersson, Hydro- and hemodynamic effects of catheterization of vessels: II. Model experiments comparing circular and annular human area reduction. *Acta Radiol. Diagnosis* 17 (1976) 749–762.
9. L. Bjorno and H. Pettersson, Hydro- and hemodynamic effects of catheterization of vessels: III. Experiments with a rigid-walled model. *Acta Radiol. Diagnosis* 18 (1977) 1–16.
10. S. Hellsten and H. Pettersson, Hydro- and hemodynamic effects of catheterization of vessels: IV. catheterization in the dog. *Acta Radiol. Diagnosis* 18 (1977) 17–24.
11. L. Bjorno and H. Pettersson, Hydro- and hemodynamic effects of catheterization of vessels: V. Experiments and clinical catheterization of stenosis. *Acta Radiol. Diagnosis* 18 (1977) 193–209.
12. D.A. MacDonald, Pulsatile flow in a catheterized artery. *J. Biomech.* 19 (1986) 239–249.
13. R.K. Dash, G. Jayaraman and K.N. Mehta, Estimation of increased flow resistance in a narrow catheterized artery - a theoretical model. *J. Biomech.* 29 (1996) 917–930.
14. A. Sarkar and G. Jayaraman, Correction to flow rate - pressure drop relation in coronary angioplasty: steady streaming effect. *J. Biomech.* 31 (1998) 781–791.
15. G.T. Karahalios, Some possible effects of a catheter on the arterial wall. *Med. Phys.* 17 (1990) 922–925.
16. G. Jayaraman and K. Tiwari, Flow in a catheterized curved artery. *Med. & Biol. Engng. & Compt.* 33 (1995) 1–6.
17. R.K. Dash, G. Jayaraman and K.N. Mehta, Flow in a catheterized curved artery with Stenosis. *J. Biomech.* 32 (1999) 49–61.
18. G. Jayaraman and R.K. Dash, Numerical study of flow in a constricted curved annulus: an application to flow in a catheterized artery. *J. Engng. Math.* (2001) in press.
19. J.F. Heyda, A Green's function solution for the case of laminar incompressible flow between non-concentric circular cylinders. *J. Franklin Inst.* 267 (1959) 15–34.
20. W.T. Snyder and G.A. Goldstein, An analysis of fully developed laminar flow in an eccentric annulus. *A.I.Ch.E. J.* 11 (1965) 462–467.
21. D.A. MacDonald, Fully developed incompressible flow between non-coaxial circular cylinders. *J. Appl. Math. Phys.* 33 (1982) 737–751.
22. L. Borges, and P. Daripa, A fast parallel algorithm for the Poisson equation on a disk. *J. Comp. Phys.* 169 (2001) 151–192.
23. P. Daripa and D. Mashat, Singular integral transforms and fast algorithms. *Num. Algor.* 18 (1998) 133–157.
24. P. Daripa, A fast algorithm to solve nonhomogeneous Cauchy-Riemann equations in the complex plane. *SIAM J. Sci. Stat. Comp.* 13 (1992) 1418–1432.
25. D.A. McDonald, *Blood Flow in Arteries*. London: Edward Arnold (1974) 496pp.